Infrared Complex Refractive Index of N-containing astrophysical ices free of water processed by cosmic-ray simulated in laboratory

W.R.M. R M Rocha, S. Pilling, A. Domaracka, H. Rothard, P. Boduch

Graphical Abstract

Infrared Complex Refractive Index of N-containing astrophysical ices free of water processed by cosmic-ray simulated in laboratory

W. R. M. Rocha,S. Pilling,A. Domaracka,H. Rothard,P. Boduch

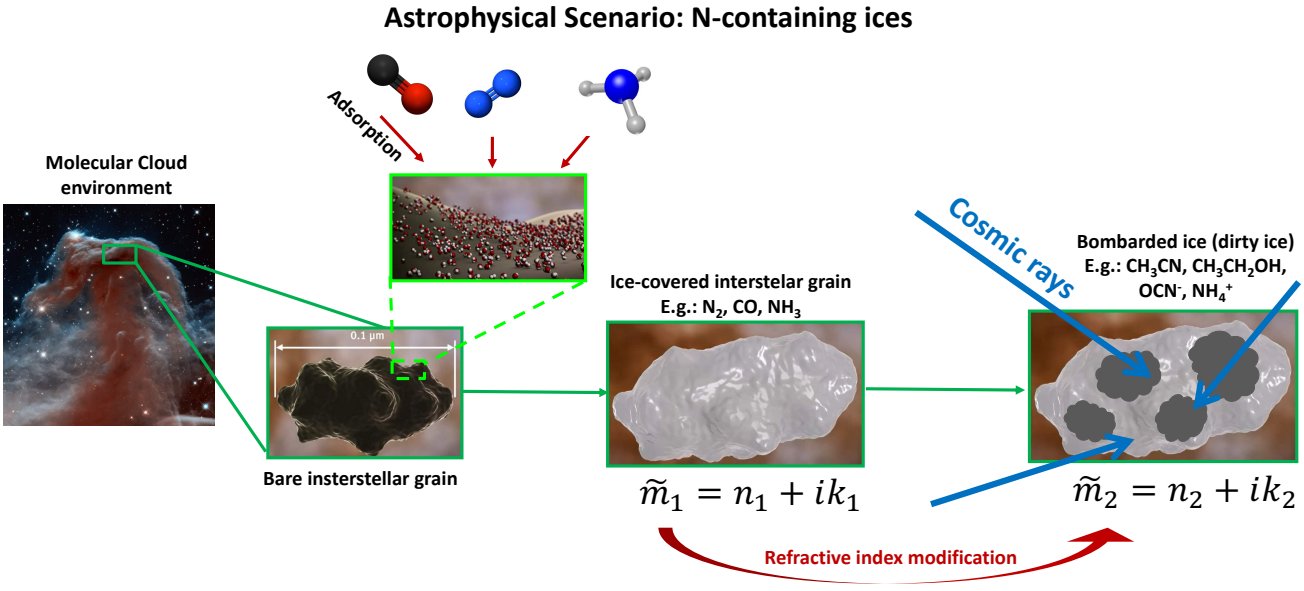

Highlights

Infrared Complex Refractive Index of N-containing astrophysical ices free of water processed by cosmic-ray simulated in laboratory

W. R. M. Rocha,S. Pilling,A. Domaracka,H. Rothard,P. Boduch

- Complex refractive index is key parameters in radiative transfer models of dusty media
- The dataset provided in this paper reduces the lack of data for the astrochemical community
- In general, the refractive index modification triggered by cormic-ray bomabardment, leads to an albedo decreasing in the infrared.

Infrared Complex Refractive Index of N-containing astrophysical ices free of water processed by cosmic-ray simulated in laboratory

W. R. M. Rocha[a,*,1], S. Pilling[a,b], A. Domaracka[c], H. Rothard[c] and P. Boduch[c]

[a]Universidade do Vale do Paraíba (UNIVAP), Laboratório de Astroquímica e Astrobiologia (LASA), Av. Shishima Hifumi, 2911, Urbanova, CEP: 12244000, São José dos Campos, SP, Brazil

[b]Departamento de Física, Instituto Tecnólogico de Aeronáutica, ITA - DCTA, Vila das Acácias, São José dos Campos, 12228-900 SP, Brazil

[c]Centre de Recherche sur les Ions, les Matériaux et la Photonique, Normandie Univ, ENSICAEN, UNICAEN, CEA, CNRS, CIMAP, 14000 Caen, France

ARTICLE INFO

Keywords:
Complex refractive index
Kramers-Kronig
Thin films
cosmic rays
astrophysical ices
mid-IR albedo

ABSTRACT

Several nitrogen containing species has been unambiguously identified in the Solar System and in the Interstellar Medium. It is believed that such rich inventory of species is a result of the energetic processing of astrophysical ices during all stages of the protostellar evolution. An intrinsic parameter of matter, the complex refractive index, stores all the "chemical memory" triggered by energetic processing, and therefore might be used to probe ice observations in the infrared. In this study, four N-containing ices have been condensed in ultra-high vacuum chamber and processed by heavy ions (O and Ni) with energies between 0.2 and 15.7 MeV at the Grand Accélérateur National d'Ions Lourds (GANIL), in Caen, France. All chemical changes were monitored *in situ* by a Infrared Absorption Spectroscopy. The complex refractive index was calculated directly from the absorbance spectrum, by using the Lambert-Beer and Kramers-Kroning relations. The values containing the values will be available in a online database: https://www1.univap.br/gaa/nkabs-database/data.htm. As result, other than the database, it was observed that non-polar ices are more destroyed by sputtering than polar ones. Such destruction and chemical evolution leads to variation in the IR albedo of samples addressed in this paper.

1. Introduction

Astrophysical ices consist of frozen molecules in extraterrestrial environments inside the Solar System and beyond. Regarding to the early stages of Young Stellar Objects (YSOs), H_2O is the major contributor to the entire inventory of ices in Space[1, 2]. Ammonia (NH_3), on the other hand, is the fourth most abundant molecular specie in the solid phase as also pointed out by Öberg et al.[1].

Inside our Solar System, N-containing environments were identified in several places, such as the Saturn's moons (e.g. Titan, Iapetus, Triton), Pluto, and Ultima Thule[3, 4]. All these objects have in common a dark/red coloration that have been attributed to "tholins", namely, extended heterogeneous aromatic and aliphatic species with various degrees of nitrogen incorporation. They are synthesized when simple molecules containing, N, C, H or O are energetically processed by ionizing agents, such as ultraviolet (UV) and cosmic rays (CRs). Due to their extensive molecular conjugation, the tholins are known by their low albedo. Other than these peculiar material, simple nitrogen bearing molecules, such as N_2 has been identified in the coma of comet 67P/Churyumov-Gerasimenko, after analysis carried out by the ROSINA (Rosetta's Orbiter Spectrometer for Ion and Neutral Analysis) mass spectrometer on board the Rosetta spacecraft [5].

From a physical chemistry perspective, nitrogen exists both in reactive (e.g. N_2O, NO_3^-, NO_2^-, NH_3, NH_4^+) and non-reactive form (N_2), giving its strongest triple molecular bond ($N \equiv N$). Laboratory experiments have shown[6, 7, 8, 9, 10, 11, 12, 13], however, that energetic processing of N_2-containing ices opens several channels for new chemical reactions, allowing the formation of N-reactive species. In addition, ·NO radicals have been considered an important precursor of prebiotic molecules, and therefore might be linked to the origin of life on earth as discussed in [14, 15].

Apart of the chemical interest in N-containing ices, the complex refractive index (henceforth called CRI) is an important parameter, as it determines how the material interacts with electromagnetic radiation. In addition, it records the chemical variation triggered by the ionizing radiation such as UV, X-rays and Cosmic-rays[16, 17, 18, 19, 20, 21]. On this subject, the aim of this paper is not to provide a detailed description of the chemical synthesis after ion bombardment of the ices, but instead, to provide a new CRI database, calculated from different N-containing ice samples, and contribute to reduce the huge lack of this kind of data in the astronomical community. Moreover, the data provided will be useful in astrophysical modelling of mid-IR spectrum of ices, as well as some clue about the role of polarization level in the ice destruction by radiation.

This papers is structured as follows: section 2 described the laboratory experiments, and the methodology employed to calculate the ice thickness and the complex refractive index of the samples probed in this work. Sections 3 and 4 show the results and astrophysical implications focusing on the role of polarity and albedo of irradiated ices. The conclusions are summarized in section 5.

*Principal corresponding author

will.rocha@nbi.ku.dk (W.R.M. Rocha)

ORCID(s): 0000-0001-6144-4113 (W.R.M. Rocha)

[1]Current address: Niels Bohr Institute Centre for Star and Planet Formation, University of Copenhagen, Øster Voldgade 5-7, DK-1350 Copenhagen K., Denmark

Table 1
N-containing samples addressed in this paper. Non-irradiated species are labelled "a", whereas the letters "b" and "c" refer to the first and second level of irradiation. The samples identification, thickness, and relative destruction are shown in columns 2, 3 and 4, respectively. The laboratory conditions under which the experiments were performed are shown in the columns 5-7.

Label	Samples	d (μm)	$\Delta d/d$	Temp. (K)	Energy/Projectile	Fluence (10^{10} ions cm^{-2})	Reference
N1a	N_2:CO (1:1)	0.7 ± 0.1	0.0	14	-	0	-
N1b	N_2:CO	0.7 ± 0.1	0.0	14	5.8 MeV $^{16}O^{2+}$	120	-
N1c	N_2:CO	0.5 ± 0.1	35.6 ± 1.2	14	5.8 MeV $^{16}O^{2+}$	1000	-
N2a	N_2:CH_4 (19:1)	11.3 ± 1.0	0.0	19	-	0	[53]
N2b	N_2:CH_4	11.2 ± 0.7	2.8 ± 0.8	19	15.7 MeV $^{16}O^{5+}$	1000	[53]
N2c	N_2:CH_4	10.5 ± 0.4	16.1 ± 1.4	19	15.7 MeV $^{16}O^{5+}$	6000	[53]
N3a	NH_3:CO (1:1)	0.8 ± 0.2	0.0	14	-	0	-
N3b	NH_3:CO	0.8 ± 0.2	0.0	14	5.8 MeV $^{16}O^{2+}$	120	-
N3c	NH_3:CO	0.6 ± 0.1	20.0 ± 1.7	14	5.8 MeV $^{16}O^{2+}$	1000	-
N4a	NH_3:CH_3OH (1:1)	4.4 ± 0.4	0.0	14	-	0	-
N4b	NH_3:CH_3OH	4.4 ± 0.4	0.0	14	0.2 MeV Ni^{24+}	100	-
N4c	NH_3:CH_3OH	4.2 ± 0.3	4.6 ± 0.3	14	0.2 MeV Ni^{24+}	1000	-

Note: Initial samples according to polarity: N1a [Non-Polar:Non-Polar], N2a [Non-Polar:Non-Polar], N3a [Polar:Non-Polar] , N4a [Polar:Polar]

2. Methodology

In this work we employ a Lambert-Beer and Kramers-Kronig based code[22] in four sets of infrared spectra of N-containing peculiar astrophysical ice analogs (virgin and irradiated) obtained in the lab to determined their complex refractive index.

2.1. Laboratory experiments

The experiment simulating bombardment of cosmic rays and energetic particles on four peculiar N-containing ices was performed by using the high-vacuum chamber mounted at the IRRSUD (IR Radiation SUD) beamline at the Grand Accelerateur National d'Ions Lourds (GANIL) located in Caen, France. Briefly, the incoming ions impinge perpendicularly the solid samples, previously produced from gas mixture and deposited over a ZnSe substrate coupled to the helium closed-cycle cryostat inside the vacuum chamber. In-situ Fourier-transformed infrared (FTIR) spectra of the sample were recorded before irradiation and at different ion fluences, using a Nicolet FTIR spectrometer (Magna 550). The ion flux was around 7×10^9 cm^{-2} s^{-1}. During the experiments, the chamber pressure was roughly 2×10^{-8} mbar. More details of the experimental set up is given in Vasconcelos et al.[12] and Pilling et al.[23].

This work presents data from 4 different experiments: 1) N_2:CO (1:1) ice at 14 K irradiated by 5.8 MeV O^{2+}, 2) N_2:CH_4 (19:1) ice at 19 K irradiated by 15.7 MeV O^{5+}, 3) NH_3:CO(1:1) ice at 14 K irradiated by 5.8 MeV O^{2+} and, 4) NH_3:CH_3OH (1:1) at 14K irradiated by 0.2 MeV Ni^{24+}. The absorbance infrared spectra of these ice mixtures are shown in Figure 1, and some assignments taken from [24] and [12] are indicated. Table 1 presents additional parameters of the addressed N-containing samples.

2.2. Initial ice thickness

The thickness of the samples listed in Table 1 before the irradiation was analytically calculated using the equations below:

$$d(\mu\text{m}) = \left[\frac{N}{\rho}\frac{M}{N_A}\right] \times 10^4 \tag{1a}$$

$$N(\text{cm}^{-2}) = \frac{2.3}{A}\int_{\nu_1}^{\nu_2} Abs_\nu d\nu \tag{1b}$$

where N is the column density (cm^{-2}), ρ the specific density (g cm^{-3}), M the molar mass, N_A Avogrados's number, A the band strength of the of molecular bond and Abs_ν the measured absorbance in the infrared spectral range.

For the N_2:CO mixture, the band centered at 2139 cm^{-1} ($\sim$ 4.67 μm) corresponding to C-O stretching mode, was used to calculate the initial thickness. The band strength (1.1×10^{-17} cm molecule^{-1}) and density (0.8 g cm^{-3}) was taken from Hudgins et al.[16] and Luna et al.[19], respectively. As N_2 has no active vibrational mode in IR, the thickness relative to nitrogen was assumed to be the same as that of CO.

In the case of N_2:CH_4 sample, the combination mode $\nu_1 + \nu_4$ of CH_4 was used to calculate the initial thickness. The band strength and density for this mixture were taken from Bouilloud et al. [25], respectively, as 3.5×10^{-19} cm molecule^{-1} and 0.45 g cm^{-3}.

The initial thickness of NH_3:CO, was calculated from the bands centered at 1070 cm^{-1} ($\sim$ 9.35 μm) relative to NH_3 (ν_2) and 2139 cm^{-1} ($\sim$ 4.67 μm) belonging to CO. The density and band strength used in this calculation for NH_3 was, respectively, 0.7 g cm^{-3} and 1.7×10^{-17} cm molecule^{-1}, as taken from Giuliano et al. [26], whereas for CO, the parameters of Section 2.2.1 have been used.

For the last sample, NH_3:CH_3OH, the vibrational modes

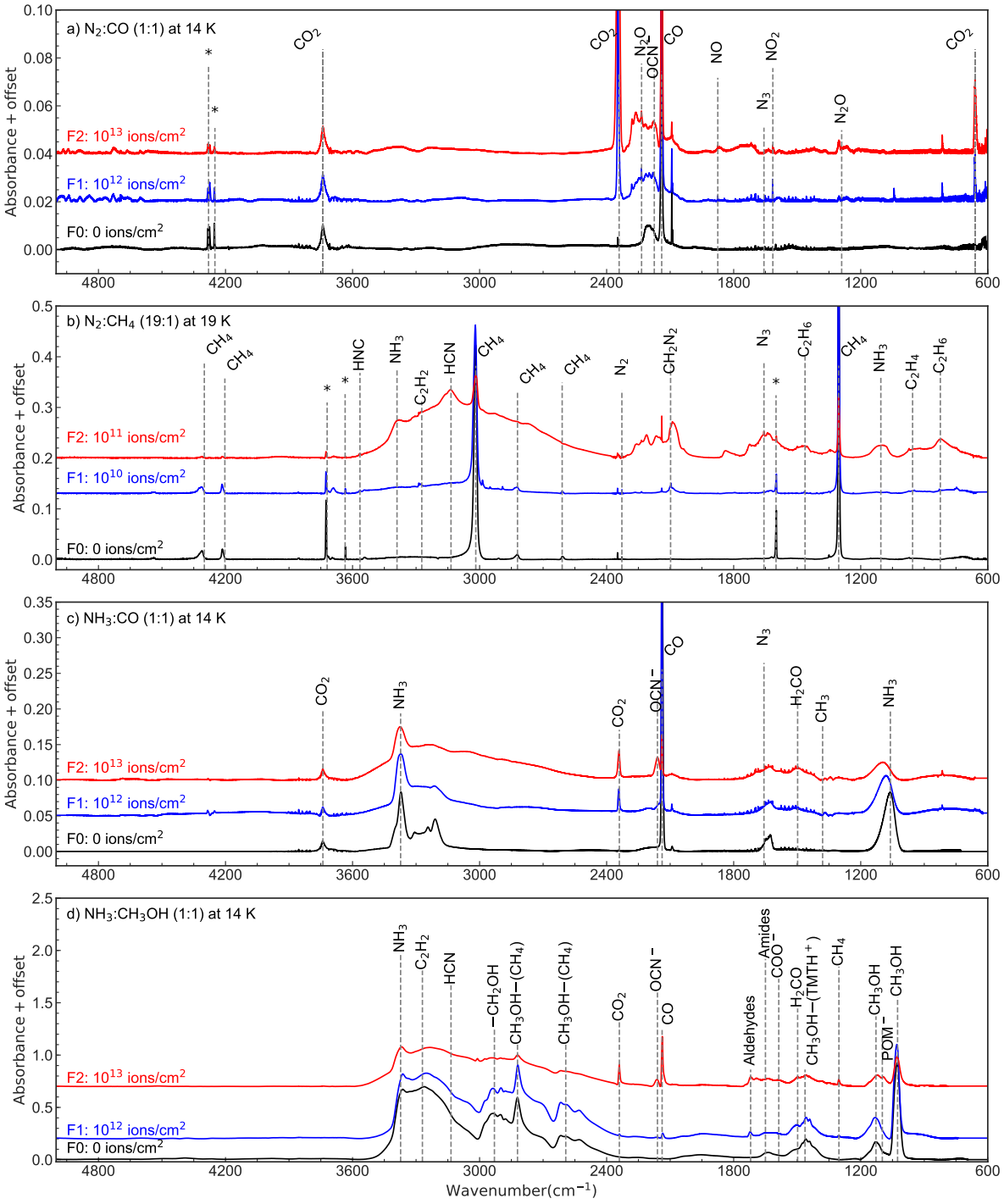

Figure 1: Absorbance infrared spectra of the four ice mixtures addressed in this paper. In order to assure a better readability, an arbitrary offset has been applied. The colours black, blue and red refer to the different fluences used in each experiment. Some vibrational modes associated to the bands are indicated by the vertical dashed grey line and their assignments is shown, as taken from [12, 24]. In the panel *d*, some bands are associated to different functional groups of molecules in literature, and are indicated by the chemical formula inside the parenthesis.

ν_4, ν_5, ν_6 and ν_7 at 1461 cm^{-1} ($\sim$ 6.84 μm) of CH_3OH, has been used to calculate the methanol thickness in this sample. As described in Giuliano et al.[26], the band strength and density of methanol ice are, respectively, 1.2×10^{-17} cm molecule^{-1} and 1.02 g cm^{-3}. For the ammonia thickness, the parameters described in the above paragraph were used.

2.3. Thickness variation

During the ice irradiation by heavy ions, the sample thickness decreases due to compaction and sputtering as widely

discussed in literature [27, 28, 29, 30].

In this paper, the compaction and sputtering model introduced in Dartois *et al.*[30], has been applied to estimate the sputtering yield (Y_S) for each experiment. Briefly, the model assumes that if a chemical species is radiolytically resistant, their column density evolution at each fluence (F) can be modelled by the following equation:

$$N(F) = N_D \times \ln\left(e^{-\frac{Y_S^{\infty} F}{N_D} + \ln\left(e^{\frac{N_0}{N_D}} - 1\right)} + 1 \right), \quad (2)$$

where N_D is the ice column density where the sputtering effect ends, and N_0 is the initial column density. The term Y_S^{∞} is the sputtering yield at an asymptotic regime, calculated from:

$$Y_S(N) = Y_S^{\infty}\left(1 - e^{-\frac{N}{N_D}}\right) \quad (3)$$

It is worth to note, however, that a radiolytically resilience property do not belong to all chemical species, and therefore, the Equation 2 applied to these situation, provides the upper limit for Y_S^{∞}.

The compaction effect, on the other hand, dominates for fluences below 10^{11} ions cm^{-2}, as pointed out in Dartois *et al.*[28]. As the data used in this paper only take into account fluences above 10^{12} ions cm^{-2}, the measured absorbances probe the real thickness evolution.

Figure 2, shows the sputtering model applied to column density variation as the fluence increases. The fitted values for N_D and Y_S^{∞} are shown inside each panel.

The ices used to calculate the column densities of the Figures 1a-1d where CO, CH_4, CO and NH_3, respectively. As shown in Pilling *et al.*[23] and Vasconcelos *et al.*[12], these molecules are not radiolytically resistant, as their column densities drastically change with the fluence, and N_D and Y_S^{∞} must be taken as upper limits.

2.4. Theoretical methodology for the complex refractive index calculation

In order to calculate the Complex Refractive Index (CRI) given by $\tilde{m} = n + ik$, the NKABS code[22] has been used. It is an interactive code, that uses the Lambert-Beer and Kramers-Kroning equations to find accurate values of CRI from the Absorbance data (Abs_ν) at different wavenumbers ν - often called frequency.

To start the code, a few parameters must be provided, such as the sample thickness (d), the refractive index at 670 nm (n_0), and for the substrate used during the experiments (n_2). The Mean Average Percentual Error (MAPE) is used to estimate the accuracy of each iteration.

The imaginary term (k) is calculated from the Lambert-Beer absorption coefficient (α), given by:

$$\alpha = \frac{1}{d}\left[2.3 \times \mathrm{Abs}_\nu + ln\left|\frac{\tilde{t}_{01}\tilde{t}_{12}/\tilde{t}_{02}}{1 + \tilde{r}_{01}\tilde{r}_{12}e^{2i\tilde{x}}}\right|^2\right] \quad (4a)$$

$$\alpha = 4\pi\nu k \quad (4b)$$

where $\tilde{t}$ and $\tilde{r}$, are the transmission and reflection Fresnel's coefficients, respectively. The sub-indexes 01, 12 and 02 are related to the interfaces vacuum-sample, sample-substrate and vaccum-substrate, respectively. The complex number in the power is directly proportion to CRI, and is given by $\tilde{x} = 2\pi\nu d\tilde{m}$.

Once the imaginary term has been determined, the real part (n) is calculated using the Kramers-Kroning relations:

$$n(\nu) = n_0 + \frac{2}{\pi}\wp\int_{\nu_1}^{\nu_2}\frac{\nu' k(\nu')}{\nu'^2 - \nu^2}d\nu' \quad (5)$$

where $\wp$ is the Cauchy Principal Value, used to solve integrals with singularity, that is this case occurs at $\nu'^2 = \nu^2$. As this integral is numerically calculated, the Maclaurin's method[31] is used to avoid such singularity. The adopted values for n_0 were 1.20 in the N1# and N2# cases and 1.30 taken from Luna et al.[19], and Hudigins et al.[16]. In all cases the substrate refractive index was 2.54.

The experimental parameters ρ, A and n_0 are the main source of error in calculating the CRI. In this sense, the error propagation was calculated by using the equations below:

$$\sigma_n^2 = \sigma_{n_0}^2 + \sigma_k^2 \quad (6a)$$

$$\sigma_k^2 = \left(\frac{\partial\alpha}{\partial d}\right)^2\sigma_d^2 \quad (6b)$$

$$\sigma_d^2 = \left(\frac{\partial d}{\partial N}\right)^2\sigma_N^2 + \left(\frac{\partial d}{\partial\rho}\right)^2\sigma_\rho^2 \quad (6c)$$

$$\sigma_N^2 = \left(\frac{\partial N}{\partial A}\right)^2\sigma_A^2 \quad (6d)$$

As such experimental parameters used in this paper are very sensitive to the chemical composition as shown in Luna *et al.*[19, 21], the values of σ_ρ, σ_A and σ_{n_0}, were estimated from the confidence limits (See Appendix). Due to uncertainties involved in the initial parameters, the error for n and k were around 12%.

3. Results and Discussion

3.1. Refractive Index in infrared

Figures 3 and 4 show the real and imaginary parts of the complex refractive index in the infrared (5000 - 600 cm^{-1}), corresponding to 2.0 - 16.6 μm. The values obtained from different irradiation levels are shown by the colours black, blue and red, respectively.

The decreasing and increasing of the band areas in Figures 3 and 4 are, respectively, related to the destruction and formation of chemical species during the irradiation process, which consequently changes the values of n and k, for virgin and processed ices.

Using accurate values for n_{670} and thickness (d), is important to determine n and k. However, the instrumentation

[1]The database containing these values in ASCII (American Standard Code for Information Interchange) format are available online at: https://www1.univap.br/gaa/nkabs-database/data.htm

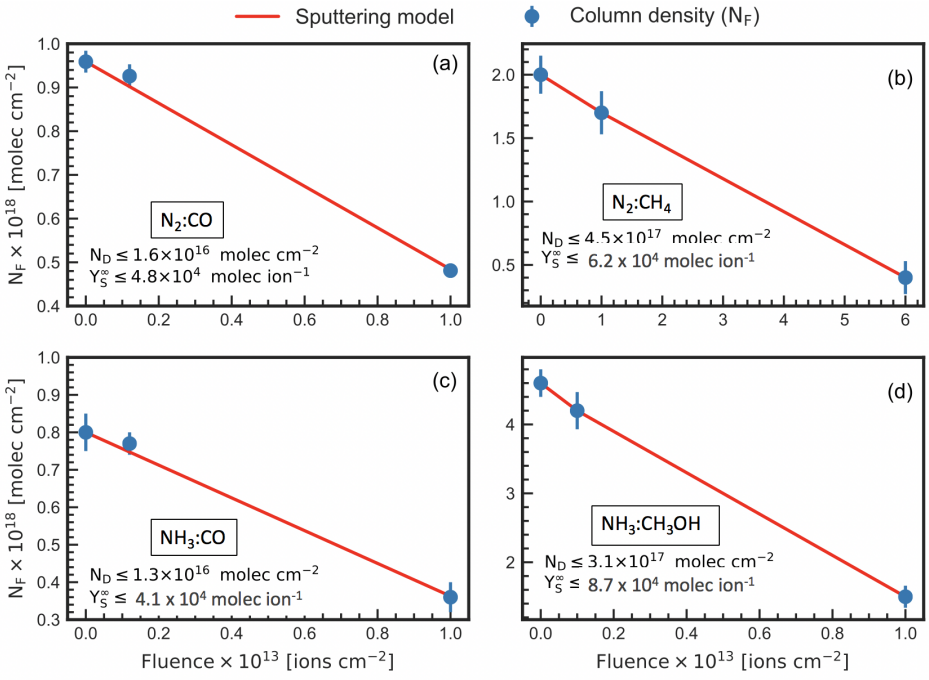

Figure 2: Column density as function of fluence for the samples studied in this paper. Each blue dot was estimated from the Absorbance data collected after the experiments (see Section 2.2). The red line is the fitting using a sputtering model detailed in Dartois et al.[30]. N_D and Y_S^∞ are the column density probed by sputtering, and the sputtering yield at the asymptotic level, respectively.

required to calculate these parameters might not be available in some laboratories. In such cases, an analytical method using averaged values has been used[23, 32] instead. In order to address the impact of approximated values in the Complex Refractive Index calculation, a statistical analysis was performed.

As result, the confidence limit of 1σ allows a variation of 30% of thickness around the mean, but only of 7% of n_0. The density and band strength allows variations around 20% and 10%, respectively.

3.2. Relative destruction

The electronic sputtering yield (Y_S), assumed here to be the main trigger of ice destruction, roughly increases quadratically with the electronic stopping power (S). Furthemore, S is a function of energy, mass and charge of a particle[33, 34, 35, 36, 30]. For instance, such dependence might be observed in the yield values in Figure 2, where Y_S of sample bombarded by Ni^{24+} is higher than for samples bombarded by O^{2+} or O^{5+}.

The effects of electronic sputtering is shown in Figure 5 in terms of the relative destruction, i.e. $\Delta d/d$ and fluence for all samples in Table 1. This figure also shows that two linear fits are required as can be seen from the solid red lines. For comparison, the black dashed lines indicates the relative destruction of H_2O-rich ices taken from Rocha et al.[20] both for polar-containing ices and non-polar containing ices, as the van der Walls force are different. The blue and green shaded areas were also taken from Rocha et al.[20]. One can observe, in fact, that such relation with the polarity found for H_2O-containing ices is also observed for N-rich ices. As described in Table 1, the samples N1a and N2a are composed by two non-polar molecules, whereas in N3a and N4a polar ices are present. However, if the ice is very thick, such effect cannot be observed, as it is the case of N2#. If samples sharing common characteristics are compared, instead (e.g. N1# and N3#), such polarity effects become more evident as they have almost the same initial thickness and were processed by the same ionizing agents. As N3# is more polar than N1#, the destruction behavior is more similar to polar ices than with non-polar species.

By comparing the linear fittings at fluence of 10^{13} ions cm^{-2}, of N-rich and H_2O-rich ices, the relative destruction for water-containing cases is about 30% higher compared to nitrogen-containing samples. However, for a non-polar situation, the N-rich ices are almost three times more rapidly destroyed than water-rich ices, which strength the idea that polar molecules are important to keep processed molecules in the same site to allow the radicals to react again and enrich the chemical complexity.

4. Astrophysical implications

4.1. Polarity in astrophysical ices

Astrophysical environments at very low temperatures (T $<$ 20K), and n $>$ 10^4 cm^{-3}, allow the formation of a non-polar layers of ice, mainly composed by CO and N_2 as shown by Boogert et al.[2], given their low desorption temperature[37]. Such layers, however, are formed onto a previous ice mantle made up of H_2O, CH_4 and NH_3, as consequence of the hy-

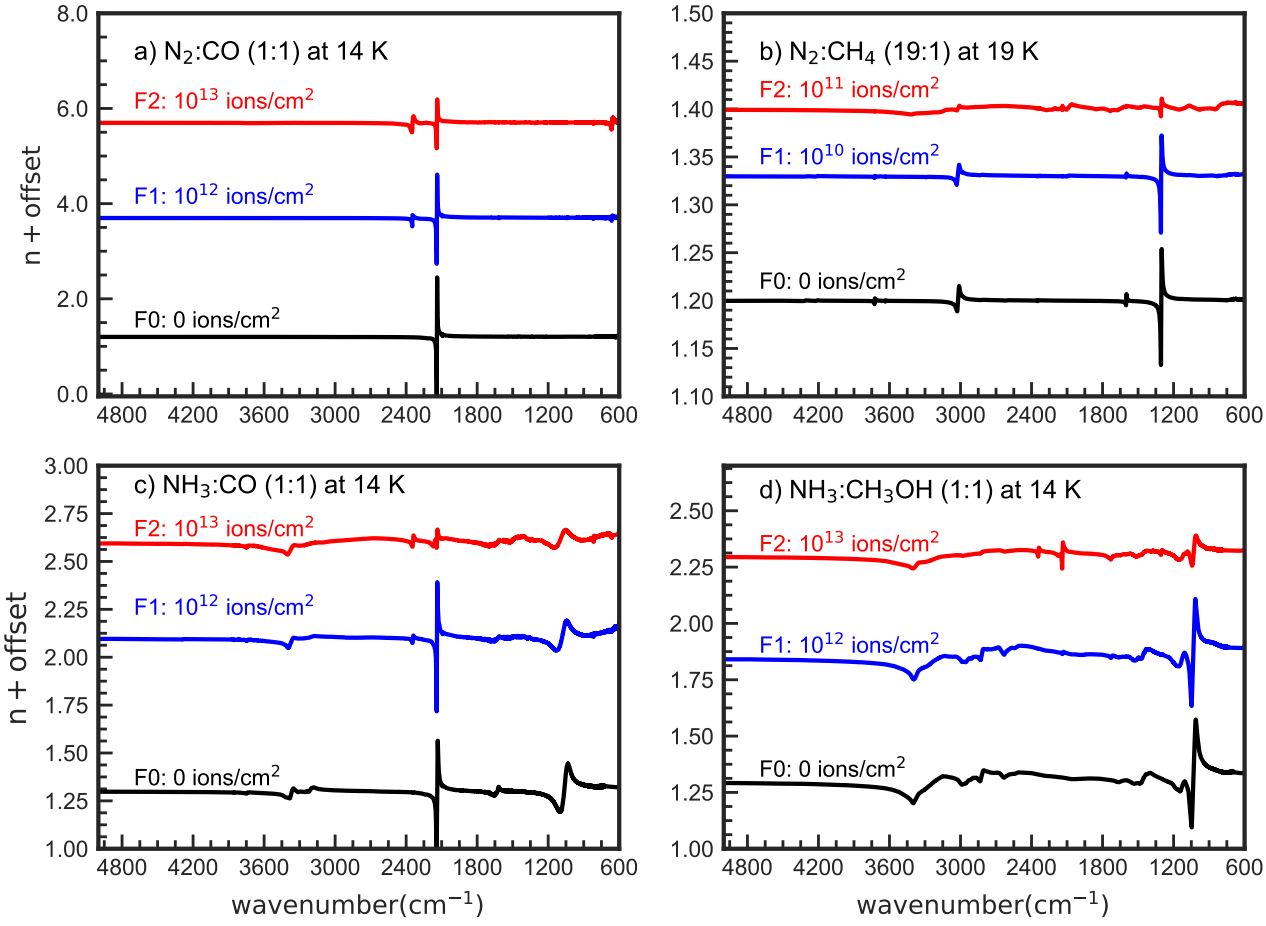

Figure 3: Real part of the Complex Refractive Index for the samples shown in Table 1 at different fluences. In order to assure a better readability, an arbitrary offset has been applied.

drogenation mechanism of small grains in Molecular Clouds[38].

Cosmic rays, on the other hand, are an important agents to enrich the chemistry in Molecular Clouds, as many endothermic reactions are forbidden due to low temperature[39]. As such energetic particles penetrate deeper than UV or X-rays photons[40] in high density regions, they reach regions where the ices are formed, leading to many physicochemical processes, including electronic sputtering, as described in Sections 2 and 3.

In such context, and assuming that non-polar ices are at least 20% more susceptible to electronic sputtering effects, as shown in Figure 5, one could expect a reduced lifetime of icy layers containing non-polar molecules. In fact, the most abundant ices in ISM are composed by H_2O, CO_2, CH_3OH, and NH_3 as shown by Öberg et al.[1]. CO ice, on the other hand, is the most abundant non-polar molecule, as also pointed out by Öberg et al.[1]. Its IR feature, however, has been attributed to CO diluted in polar-matrices of H_2O, CO_2 and CH_3OH.

Other aspects relating polarity to astrophysical ices, have also been reported by Müller et al.[41], associating the band strength of O_2 with the chemical environment. In addition, Knez et al.[42], point out that the acetylene's ν_5 feature is much more resolved in ices dominated by non-polar or low-polarity molecules.

4.2. Opacities and albedos for astrophysical models

Since the complex refractive index records the chemical evolution of astrophysical ices, they can be used to derive opacity table of dust models, which are the input of radiative transfer models dominated by dust. In fact, previous works by [43, 44, 45, 46, 47], have shown that the IR spectrum of YSOs are better reproduced by grain model combining dust and ice opacities. Other than ISM, where the standard ice model is dominated by H_2O[1, 2], some places in the Solar System are dominated by N-containing ices, such as Saturn's moons (e.g. Titan, Iapetus, Triton), Pluto, and Ultima Thule[3, 48, 4]

Another direct astrophysical implication of cosmic ray irradiation of N-containing ices, is related to the albedo changes with the chemistry. The generic albedo, can be given by the

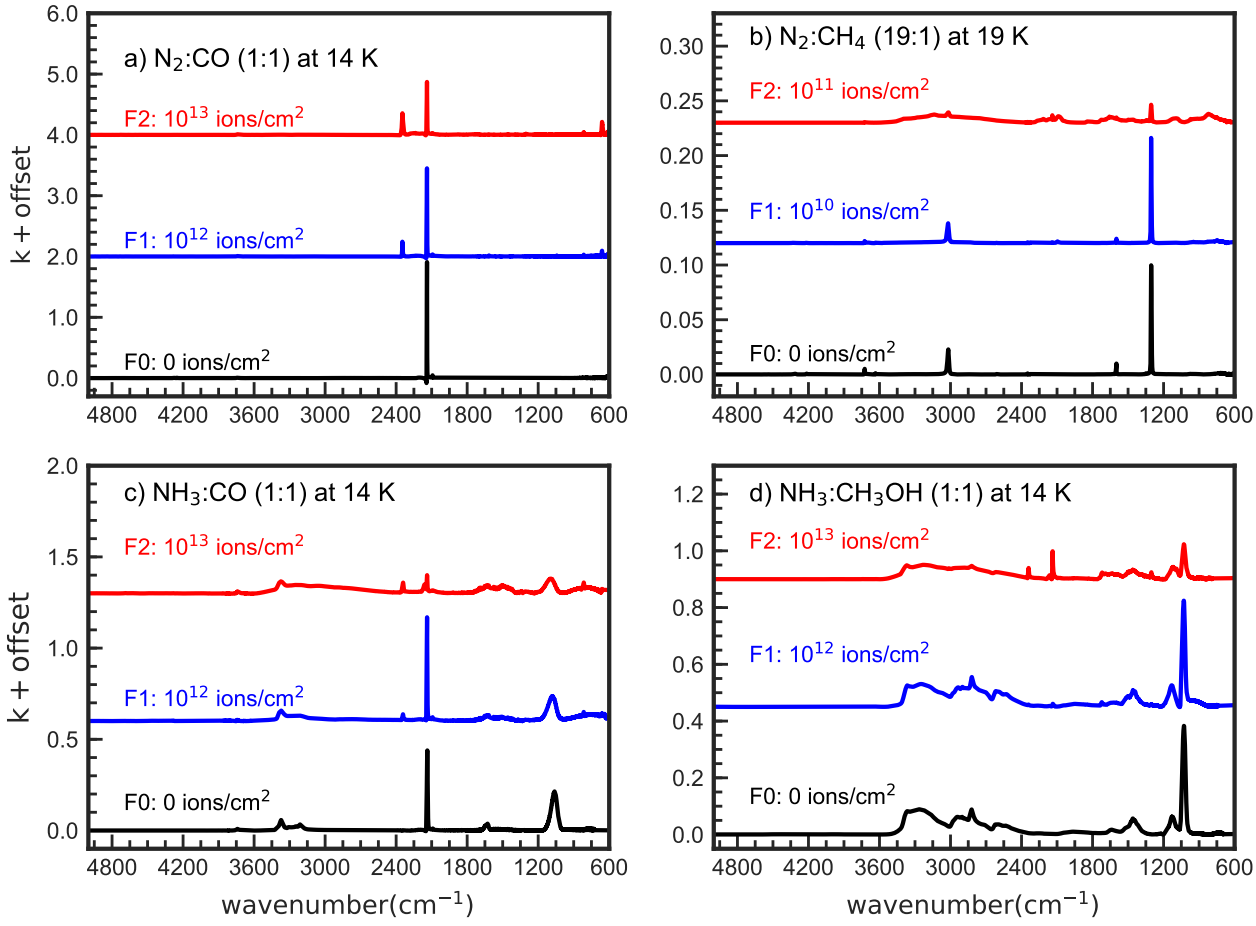

Figure 4: Imaginary part of the Complex Refractive Index for the samples shown in Table 1 at different fluences. In order to assure a better readability, an arbitrary offset has been applied.

following equation as defined in Hanner et al.[49]:

$$\omega(\theta, \lambda) = \frac{\phi(\theta)}{x^2} \tag{7}$$

where $\phi(\theta)$ is the dimensionless scattering function, and x is the size parameter. Both equations are defined by:

$$\phi(\theta) = \frac{4\pi}{k_{scat}} Z_{11}(\theta) \tag{8a}$$

$$x = \frac{2\pi a}{\lambda} \tag{8b}$$

where k_{scat} is the scattering opacity in cm^2 g^{-1}, $Z_{11}(\theta)$ are the values from the scattering matrix in cm^2 g^{-1} sr^{-1} calculated from a full scattering Muller matrix for all angles of scattering (see Bohren & Huffman[50] for details), and θ is the phase angle. The subindex '11' means the intensity from the Stokes parameter[2]. The geometric albedo, on the other hand, is defined as the ratio between the scattered light at zero phase angle and the scattering of a idealized lambertian surface of same cross section. In another approach, the geometric albedo is also defined as two thirds of the single-scattering albedo, given by:

$$\eta = \frac{k_{scat}}{k_{abs} + k_{scat}} \tag{9}$$

where k_{abs} is the scattering opacity in cm^2 g^{-1}. The sum $k_{abs} + k_{scat}$ is known as extinction opacity (k_{ext}).

In order to address the geometric albedo variation due to the chemical changes induced by the energetic processing of ices, a computational code in Python programing language was used[3]. Briefly, this code uses the Mie theory[51] to solve Maxwell's equation for the light dispersion in a medium containing spherical particles. Figure 6 show the geometric albedo of the samples addressed in this paper, as function of the wavelength, fluence, and grain size. Different particle radius are used to highlight the scattering effects from small to large grains. The trend between geometric albedo

[2]As the polarization effect is not addressed in this study, the other Stokes parameters Q, U, and V are not being considered.

[3]Note by C. Dullemond: This is a python version of the famous Bohren Huffman Mie code. It was ported to Python from its original version bhmie.f (written by Bruce Draine) by Cornelis Dullemond, February 2017. Available in: http://www.ita.uni-heidelberg.de/ dullemond/software/radmc-3d/

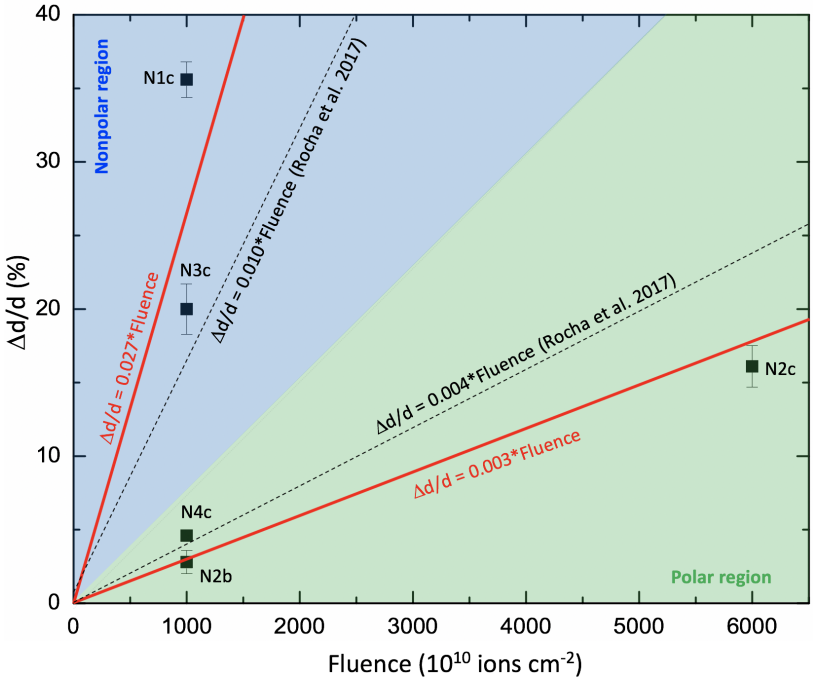

Figure 5: Relative destruction variation (in percentage) against fluence. The squares are the values for each sample in Table 1. The red solid lines are the fittings assuming a linear approximation for the N-rich ices. The black dashed lines are the fittings for H_2O-rich ices taken from Rocha et al.[20]. Both polar and non-polar regions are identified by a green and blue shaded region.

and fluence is not universal for the samples shown in Figure 6, although one can note a general trend of decreasing in different wavelenghts. The ice mixture NH_3:CH_3OH diverge from the decreasing trend (panels d, h, l), since the geometric albedo at Fluence 3 is higher than in Fluence 2 between 2.9 and 4.2 μm. Such a relationship between geometric albedo and fluence is given by the synthesis of complex molecules, including several saturated or non-saturared aliphatic compounds[12], and heteropolymers[52]. In the former case, however, the disarranged polymer-like structure and the complex combinations of functional groups has been called "tholins", as coined by Sagan & Khare[53], and are responsible for the low albedo and reddish colour associated to these compounds[54]. The existence of tholins in our samples, however, has not been addressed yet, and will be investigated in a future manuscript. The grain size dependence, in general, decrease the geometric albedo in all wavelengths, although this effect is more prominent for particle radius of 100μm (panels i,j,k,l). Particularly, both O——H bonds and ammonia hydrates affects the bands in the spectral range shown in Figure 6. Additionally to the chemistry, nevertheless, large grains cause an extra extinction due to scattering for $\lambda > 3.1$ μm as reported by Léger et al.[55], that's particularly the case of particle radius of 10 μm (middle column), compared to 1 μm (left column). For very large grains, however, it worth to describe the limts of the Mie theory applied to scattering effects. This limit is given by the non-dimensional size parameter given by Equation 8b. In terms of the single scattering albedo and the CRI calculated in this paper, $x > 200$ characterizes the geometric optics limit, whereas $0.2 < x < 200$ the Mie theory is fully considered[56]. For $x < 0.2$ the Rayleigh regime is adopted. In the case of 100 μm icy grain radius, the range below 3 μm is in the geometric optics limit, and must be used with caution. The range above 3μm, however, can be fully considered.

Figure 9 show the the geometric albedo as function of the wavelength, fluence, and grain size for the range between 5 and 8 μm. This spectral range contains contributions of several functional groups associated to complex species such as alcohols, aliphatic ethers (R1-OCH_2-R2) and related molecules[2]. As observed in Figure 6, both the fluence and grain size increasing, reduce the icy grain geometric albedo, except in specific spectral intervals in the case of NH_3:CH_3OH. For example, the geometric albedo in the the range between 6.5 μm and 7.2 μm for grain radius of 1 μm and 10 μm, is higher than the samples at Fluence 0 and Fluence 1. Nevertheless it is an unexpected result, since one could expect an albedo reducing due to the synthesis of more complex species with the irradiation exposure, this suggest that the production of complex molecules do not increases with all levels of irradiation in some cases, but rather, high fluences might destroy the chemical bonds of synthesized species formed earlier in the same experiment. In terms of scattering regime, the interval between 5 and 8 μm for large particle radius (100 μm) ramains in the Mie regime, although very close of the geometric optics domain. The extinction caused by scattering in this case still very prominent, and reduces the geometric albedo by a factor of 4−6 for $5.8\mu m < \lambda < 7.2\mu m$.

The relative and integrated geometric albedo changes with

the chemical processing and particle size for the cases between 2.0−5.0 μm and 5.0−8.0 μm is shown in Figures 8 and 9, respectively. The ice mixtures N_2:CO, NH_3:CO and NH_3:CH_3OH are shown in the upper panels, whereas N_2:CH_4 is shown in the bottom panels, since it was irradiated in a different fluence regime, and also because this sample do not contains Oxygen atoms in its structure. In Figure 8, the geometric albedo of all samples decreases with the fluence and grain size, except in the case of NH_3:CH_3OH. Apart of the small decreasing observed in panels *a* and *b* (less than 2%), its geometric albedo increases with the fluence. Differently of the O-containing ice mixtures, the normalized and integrated geometric albedo of N_2:CH_4 decreases linearly with the fluence. On the other hand, some differences are observed in the normalized and integrated geometric albedo between 5−8 μm, as shown in Figure 9. The decreasing albedo is observed for the O-containing ice mixtures, except in the case of NH_3:CH_3OH, that increases for large fluences, independent of the grain size. The role for N2:CH4 is no longer linear, as observed for the case between 2−5 μm, but show a small increasing at low fluences, and then decreases significantly for small (1 μm) and large grains (100 μm). Intermediary grain sizes, such as 10 μm, the normalized and integrated albedo remains constant, taken into account the error bars.

As a test case, the NH_3:CO geometric albedo is compared to the reflectance profile of two regions of Iapetus, a Saturn's icy moon. The Iapetus's surface has a unique bimodal albedo distribution as shown in the *top* panel of Figure 10. The white hemisphere is rich in H_2O, and show a geometric albedo of around 60%, whereas the dark region (white dashed box) is dominated by nitrogen-rich tholin (——C$\equiv$N) [57]. The origin of this dichotomy is beyond the scope of this work, but detailed explanations can be found in [58, 59]. Between these two hemispheres, a mixed region (green dashed box) has also been studied [60]. The temperature variation as seen between 9−16 μm is shown to highlight the high temperature associated to the low albedo in the dark region, compared to the H_2O-rich water. The spectrum as observed by the Visible and Infrared Mapping Spectrometer (VIMS) instrument on-board of Cassini spacecraft between 2−5 μm for the dark[61] and mixed[60] region is shown in the *bottom* panel by the solid black line. Both blue and red lines are the scaled geometric albedo (also called reflectance) taken from panel *g* in Figure 6. Only the particle radius of 10 μm is shown since it provided the best comparison by eye. The NH_3 at 3 μm and CO_2 at 4.25 μm features are prominent in this comparison, whereas other bands such as CO_2 at 2.65 μm, OCN^- at 4.62 μm and CO at 4.67 μm are not observed by VIMS, which can be caused by a resolution issue. Another feature observed in the experiments is the ^{13}CO mode at 4.73 μm, but only observed in the mixed region during the mission at 2004 July 13, but not observed at another flyby at 2004 October 7. Buratti et al.[60], however, do not comment about this band in their work. Some chemical differences are strickly between 2.5 and 4.0 μm. Since H_2O is also present in the low albedo region, the band centered in 3 μm is more broader than the transitions for NH_3:CO even at high fluences. Two regions are hatched in this papen, namely, $\lambda = 2.8\mu$m and $\lambda = 3.6\mu$m, since they are strongly affected by (C —— N) and (N —— H) bonds, although the grain size effect at $\lambda = 3.6\mu$m is also known[55].

5. Conclusions

The Complex Refractive Index of N-containing ices processed by heavy ions in the laboratory is shown in this paper. This contributes to reduce the lack of this kind of data in the astronomical community, and become useful to improve the computational simulations in environments dominated by dust and N-ice.

The relative destruction triggered by sputtering can be associated to the polarity level of ice samples, as it was also observed for H_2O-containing molecules in Rocha et al.[20]. From a astrochemical perspective, this implies in a short lifetime of non-polar mantles of ices inside Molecular Clouds. Such scenario, however, opposes to layered structure of ices, and strengthen the idea that non-polar species are triggered in a H_2O-dominated ice matrix.

The geometric albedo calculated in this paper in two wavelength windows has shown a strong dependence with the particle size and chemical processing induced by cosmic-rays analogues. The albedo decreasing observed in both cases suggest the formation of N-rich tholins and aliphatic saturated and non-saturared complex molecules, which is associated to reddish colours in small bodies of the Solar System. As a test case, the geometric albedo of NH_3:CO at two fluence levels were compared to the geoemtric albedo (reflectance) of the dark and mixed region in Iapetus, a Saturn's moon. Although the aim of this comparison was not provide a conclusive analysis of the Iapetus' surface composition, one can note that a energetic processing of N-rich component containing traces of other materials (carbon and oxygen), seems to be the likely scenario to explain the low albedo region seem by the Cassini's instruments. This becomes a strong motivation for future prospects aiming further chemical constraints of low albedo surfaces inside the Solar System and beyond.

6. Aknowledgements

The authors acknowledge the anonymous referee's comments that securely improved this manuscript. They also are grateful to the financial support provided by the Brazilian agencies FAPESP (Projects 2015/23054-7, 2016/11334-5, 2017/07283-9, 2016/22018-7 and 2013/07657-5) and CNPq (Projects 304130/2012-5 and 306145/2015-4). WRMR also acknowledge MSc. Giulia Perotti for the fruitful discussions about this paper.

A. Appendix

The degeneracy was addressed by using a χ^2 statistical analysis. In summary, random values were attributed to A, ρ, and n_0 in Equations 1a, 1b and 5, which allowed NKABS

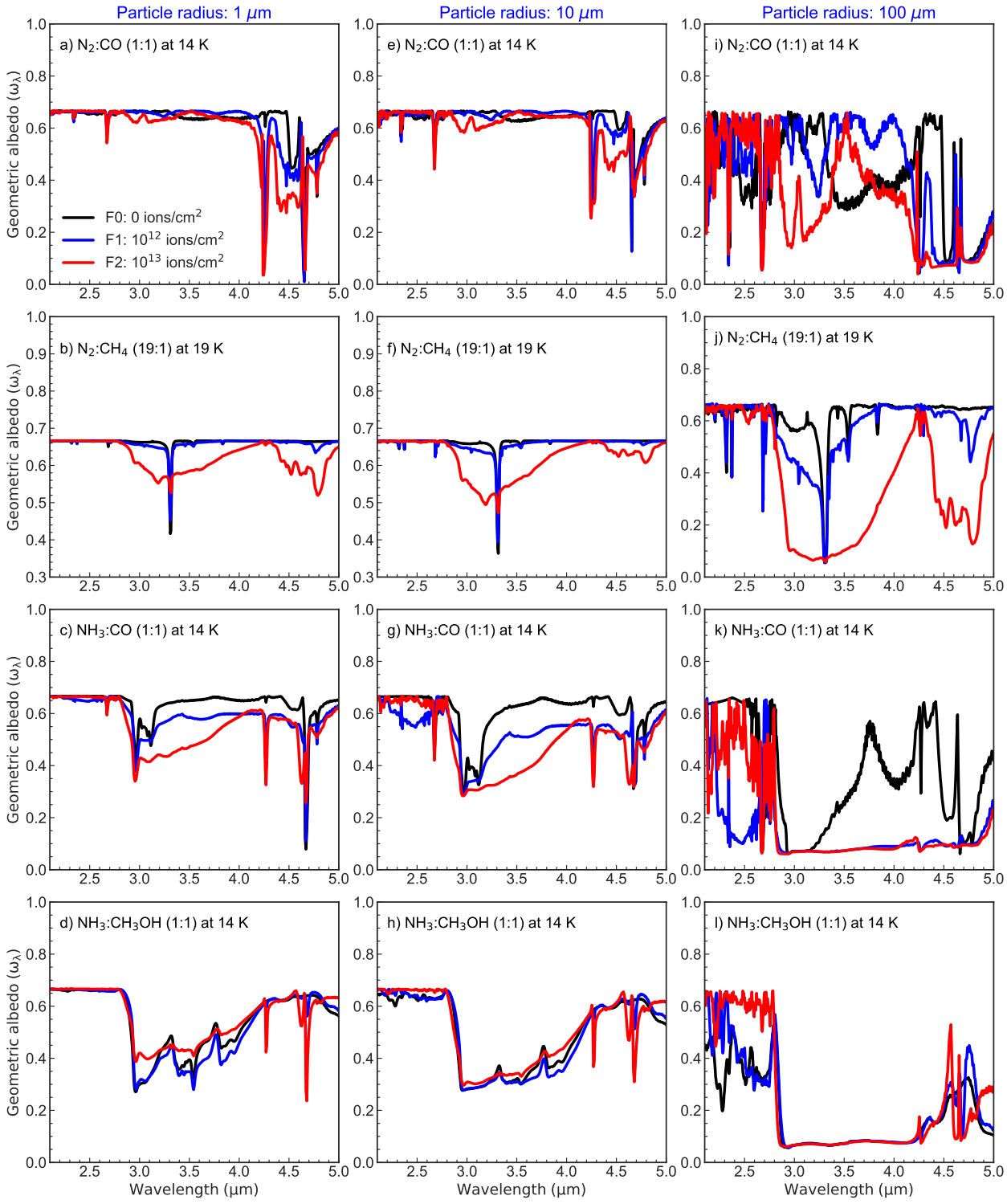

Figure 6: 2–5μm wavelength and grain size dependent geometric albedo for the ice mixtures listed in Table 1, and shown in each row from the top to bottom panels. The first, second and third columns indicate the icy grain radius of 1μm, 10μm and 100μm, respectively.

to calculate the n and k after 10 iterations, and a χ^2 given by Equation 7a was calculated.

$$\chi^2 = \sum_i \frac{\left(Abs_{v,i}^{exp} - Abs_{v,i}^{theo}\right)^2}{Abs_{v,i}^{theo}} \tag{10a}$$

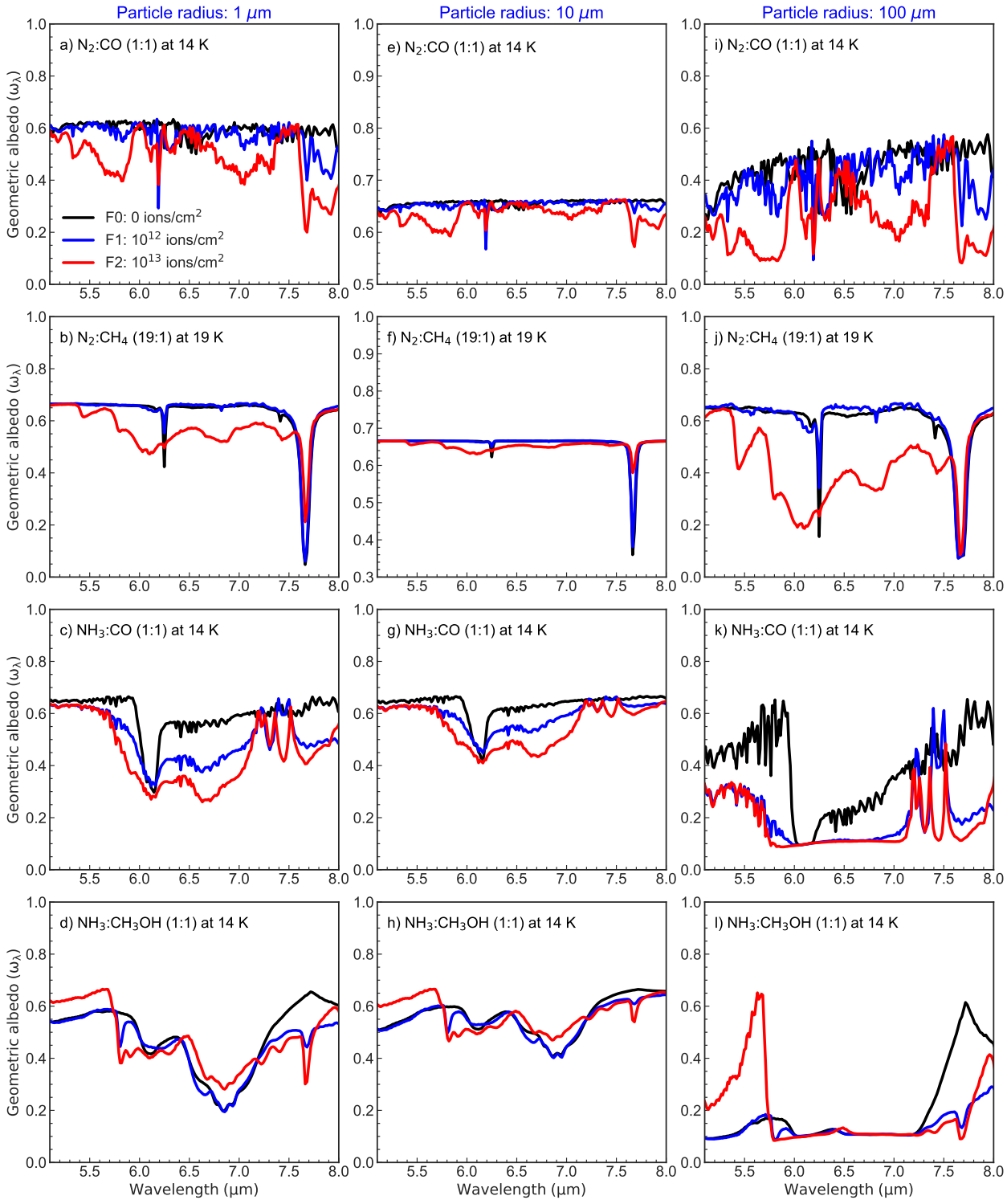

Figure 7: Same of Figure 6, but for the range between 5−8 μm.

$$Abs_{\nu,i}^{theo} = Abs(n_0, A, \rho) \tag{10b}$$

where Abs_{ν}^{exp} is the laboratory data.

At the end of 5000 simulations, a χ^2 analysis was performed, by using the following equation:

$$\Delta\chi^2(\nu, \alpha) = \chi^2 - \chi^2_{min} \tag{11}$$

where ν and α are the degrees of freedom and the statistical significance, respectively. One can observe, that confidence regions do not depend on the accuracy of the fit, but the number of degrees of freedom.

Figure 11 shows an example of this investigation for the sample N1, once the other results were similar. The colours

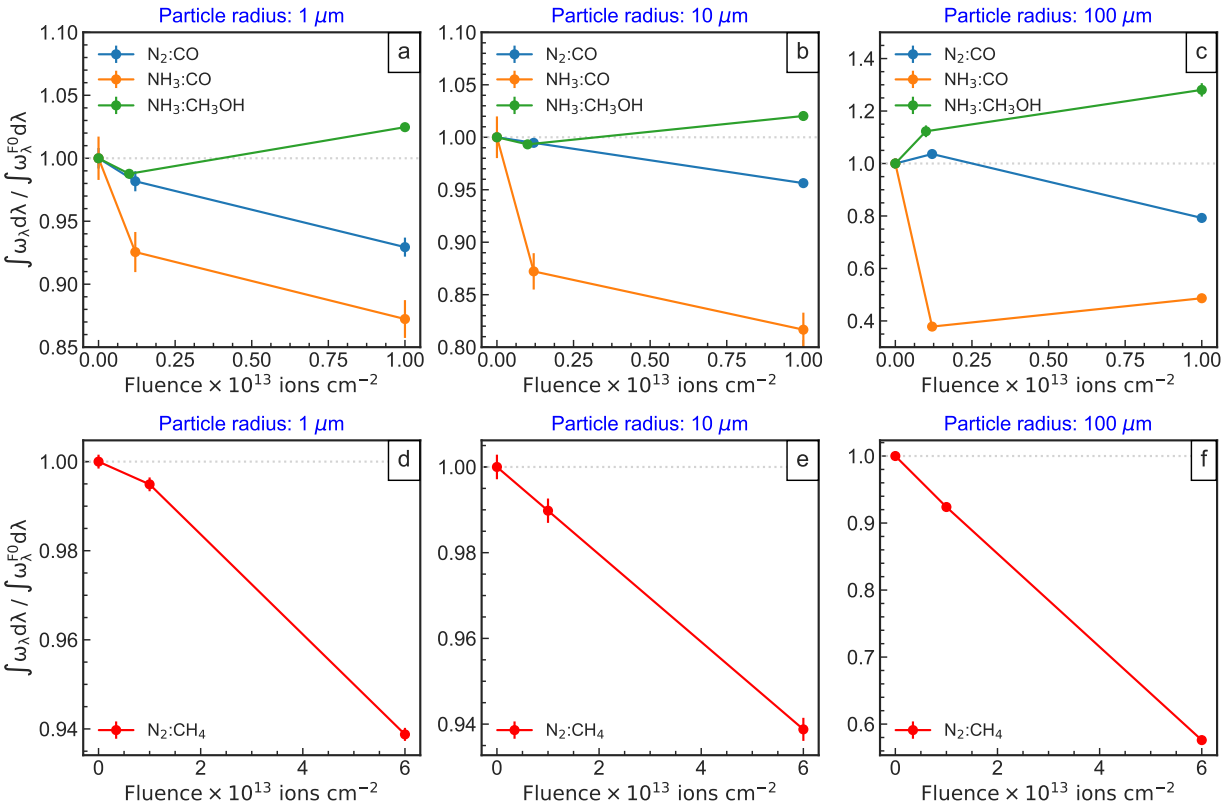

Figure 8: Normalized and integrated geometric albedo between 2−5 μm against fluence for all samples in Table 1 for 3 icy grain sizes. As the sample N2# was irradiated in a fluence range different of the other samples, it is shown separately at the bottom layer. The lines are to guide the eye only. A light gray dotted line indicate the ratio equal the unity.

show $\Delta\chi^2$ for the thickness against n_0 and Band strength against Density. The histograms are also shown, and the upper, lower and mean values are indicated. The confidence limits in terms of σ are presented by the solid white, yellow and red colours, respectively.

References

[1] K. I. Öberg, A. C. A. Boogert, K. M. Pontoppidan, S. van den Broek, E. F. van Dishoeck, S. Bottinelli, G. A. Blake, and N. J. Evans, II. The Spitzer Ice Legacy: Ice Evolution from Cores to Protostars. *Astrophys. J.*, 740:109, October 2011.

[2] A. C. A. Boogert, P. A. Gerakines, and D. C. B. Whittet. Observations of the icy universe. *Annu. Rev. Astron. Astrophys.*, 53:541–581, August 2015.

[3] D. P. Cruikshank, W. M. Grundy, F. E. DeMeo, M. W. Buie, R. P. Binzel, D. E. Jennings, C. B. Olkin, J. W. Parker, D. C. Reuter, J. R. Spencer, S. A. Stern, L. A. Young, and H. A. Weaver. The surface compositions of Pluto and Charon. *Icarus*, 246:82–92, January 2015.

[4] S. A. Stern, H. A. Weaver, and Spencer et al. Initial results from the New Horizons exploration of 2014 MU_{69}, a small Kuiper Belt object. *Science*, 364(6441), May 2019.

[5] M. Rubin, K. Altwegg, H. Balsiger, A. Bar-Nun, J.-J. Berthelier, A. Bieler, P. Bochsler, C. Briois, U. Calmonte, M. Combi, J. De Keyser, F. Dhooghe, P. Eberhardt, B. Fiethe, S. A. Fuselier, S. Gasc, T. I. Gombosi, K. C. Hansen, M. Hässig, A. Jäckel, E. Kopp, A. Korth, L. Le Roy, U. Mall, B. Marty, O. Mousis, T. Owen, H. Rème, T. Sémon, C.-Y. Tzou, J. H. Waite, and P. Wurz. Molecular nitrogen in comet 67P/Churyumov-Gerasimenko indicates a low formation temperature. *Science*, 348:232–235, April 2015.

[6] M. A. Satorre, M. E. Palumbo, and G. Strazzulla. Infrared spectra of N_2-rich ice mixtures. *J. Geophys. Res.*, 106:33363–33370, December 2001.

[7] P. Boduch, A. Domaracka, D. Fulvio, T. Langlinay, X. Y. Lv, M. E. Palumbo, H. Rothard, and G. Strazzulla. Chemistry induced by energetic ions in water ice mixed with molecular nitrogen and oxygen. *Astron. Astrophys.*, 544:A30, August 2012.

[8] G. A. Cruz-Diaz, G. M. Muñoz Caro, Y.-J. Chen, and T.-S. Yih. Vacuum-UV spectroscopy of interstellar ice analogs. II. Absorption cross-sections of nonpolar ice molecules. *Astron. Astrophys.*, 562:A120, February 2014.

[9] B. Augé, E. Dartois, C. Engrand, J. Duprat, M. Godard, L. Delauche, N. Bardin, C. Mejía, R. Martinez, G. Muniz, A. Domaracka, P. Boduch, and H. Rothard. Irradiation of nitrogen-rich ices by swift heavy ions. Clues for the formation of ultracarbonaceous micrometeorites. *Astron. Astrophys.*, 592:A99, August 2016.

[10] G. C. Almeida, S. Pilling, A. L. F. de Barros, C. A. P. da Costa, R. C. Pereira, and E. F. da Silveira. Processing of N_2O ice by fast ions: implications on nitrogen chemistry in cold astrophysical environments. *Mon. Not. R. Astronom. Soc.*, 471:1330–1340, October 2017.

[11] F. A. Vasconcelos, S. Pilling, W. R. M. Rocha, H. Rothard, and P. Boduch. Radiolysis of N2-rich astrophysical ice by swift oxygen ions: implication for space weathering of outer solar system bodies. *Physical Chemistry Chemical Physics (Incorporating Faraday Transactions)*, 19:24154–24165, 2017.

[12] F. d. A. Vasconcelos, S. Pilling, W. R. M. Rocha, H. Rothard, and P. Boduch. Energetic Processing of N_2:CH_4 Ices Employing X-Rays and Swift Ions: Implications for Icy Bodies in the Outer Solar System. *Astrophys. J.*, 850:174, December 2017.

[13] G. Fedoseev, C. Scirè, G. A. Baratta, and M. E. Palumbo. Cosmic ray processing of N_2-containing interstellar ice analogues at dark cloud

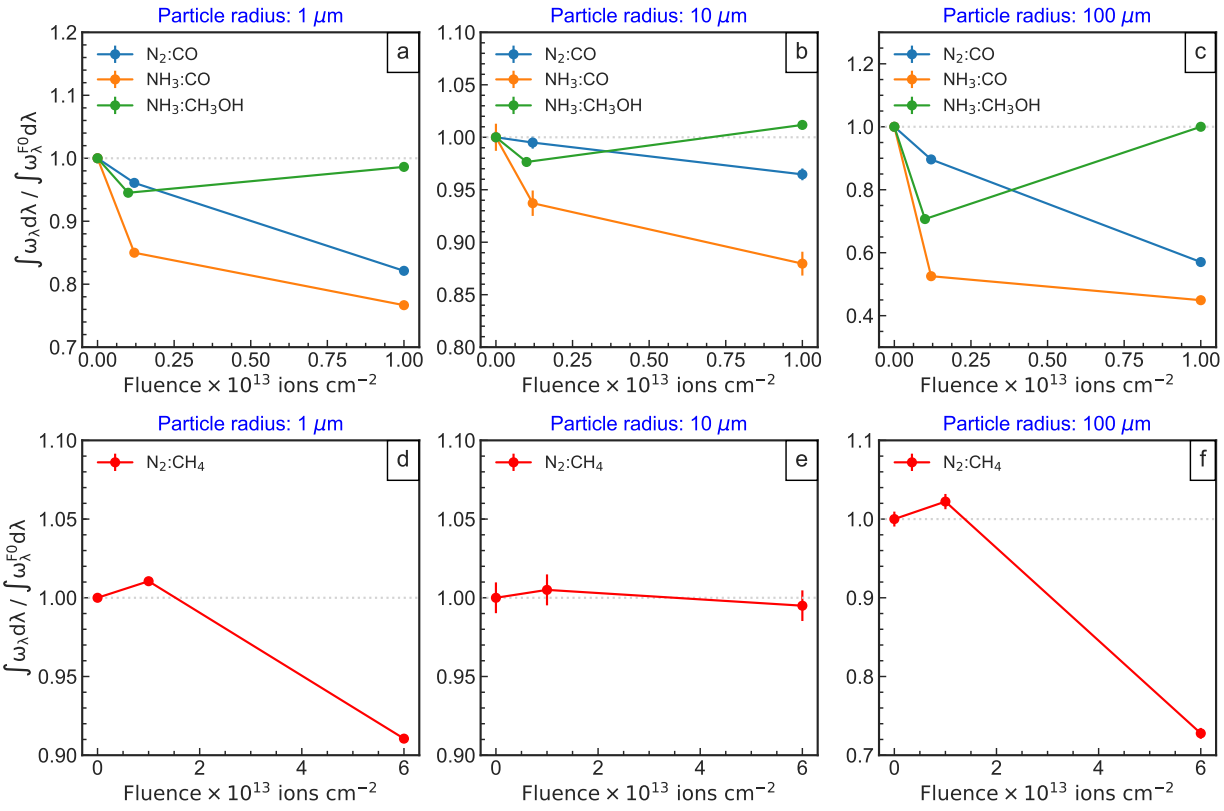

Figure 9: Same of Figure 8, but for the range between 2−5 μm.

conditions. *Mon. Not. R. Astronom. Soc.*, 475:1819–1828, April 2018.

[14] A. L. F. de Barros, E. F. da Silveira, D. Fulvio, P. Boduch, and H. Rothard. Formation of nitrogen- and oxygen-bearing molecules from radiolysis of nitrous oxide ices - implications for Solar system and interstellar ices. *Mon. Not. R. Astronom. Soc.*, 465:3281–3290, March 2017.

[15] D. Fulvio, G. A. Baratta, B. Sivaraman, N. J. Mason, E. F. da Silveira, A. L. F. de Barros, O. Pandoli, G. Strazzulla, and M. E. Palumbo. Ion irradiation of N_2O ices and NO_2:N_2O_4 ice mixtures: first steps to understand the evolution of molecules with the N-O bond in space. *Mon. Not. R. Astronom. Soc.*, 483:381–391, February 2019.

[16] D. M. Hudgins, S. A. Sandford, L. J. Allamandola, and A. G. G. M. Tielens. Mid- and far-infrared spectroscopy of ices - Optical constants and integrated absorbances. *Astrophys. J.*, 86:713–870, June 1993.

[17] P. Ehrenfreund, A. C. A. Boogert, P. A. Gerakines, A. G. G. M. Tielens, and E. F. van Dishoeck. Infrared spectroscopy of interstellar apolar ice analogs. *Astron. Astrophys.*, 328:649–669, December 1997.

[18] M. H. Moore, R. F. Ferrante, W. J. Moore, and R. Hudson. Infrared Spectra and Optical Constants of Nitrile Ices Relevant to Titan's Atmosphere. *Astrophys. J.*, 191:96–112, November 2010.

[19] R. Luna, M. Á. Satorre, M. Domingo, C. Millán, and C. Santonja. Density and refractive index of binary CH_4, N_2 and CO_2 ice mixtures. *Icarus*, 221:186–191, September 2012.

[20] W. R. M. Rocha, S. Pilling, A. L. F. de Barros, D. P. P. Andrade, H. Rothard, and P. Boduch. Infrared complex refractive index of astrophysical ices exposed to cosmic rays simulated in the laboratory. *Mon. Not. R. Astronom. Soc.*, 464:754–767, January 2017.

[21] R. Luna, G. Molpeceres, J. Ortigoso, M. A. Satorre, M. Domingo, and B. Maté. Densities, infrared band strengths, and optical constants of solid methanol. *Astron. Astrophys.*, 617:A116, September 2018.

[22] W.R.M. Rocha and S. Pilling. Determination of optical constants n and k of thin films from absorbance data using kramers-kronig relationship. *Spectrochimica Acta Part A: Molecular and Biomolecular Spectroscopy*, 123:436 – 446, 2014.

[23] S. Pilling, E. Seperuelo Duarte, E. F. da Silveira, E. Balanzat, H. Rothard, A. Domaracka, and P. Boduch. Radiolysis of ammonia-containing ices by energetic, heavy, and highly charged ions inside dense astrophysical environments. *Astron. Astrophys.*, 509:A87, January 2010.

[24] G. M. Muñoz Caro, E. Dartois, P. Boduch, H. Rothard, A. Domaracka, and A. Jiménez-Escobar. Comparison of UV and high-energy ion irradiation of methanol:ammonia ice. *Astron. Astrophys.*, 566:A93, June 2014.

[25] M. Bouilloud, N. Fray, Y. Bénilan, H. Cottin, M.-C. Gazeau, and A. Jolly. Bibliographic review and new measurements of the infrared band strengths of pure molecules at 25 K: H_2O, CO_2, CO, CH_4, NH_3, CH_3OH, HCOOH and H_2CO. *Mon. Not. R. Astronom. Soc.*, 451:2145–2160, August 2015.

[26] B. M. Giuliano, R. M. Escribano, R. Martín-Doménech, E. Dartois, and G. M. Muñoz Caro. Interstellar ice analogs: band strengths of H_2O, CO_2, CH_3OH, and NH_3 in the far-infrared region. *Astron. Astrophys.*, 565:A108, May 2014.

[27] M. E. Palumbo, G. A. Baratta, and F. Spinella. Cosmic ion irradiation and UV photolysis of solids in star forming regions . *Memorie della Societa Astronomica Italiana Supplementi*, 9:192, 2006.

[28] E. Dartois, J. J. Ding, A. L. F. de Barros, P. Boduch, R. Brunetto, M. Chabot, A. Domaracka, M. Godard, X. Y. Lv, C. F. Mejía Guamán, T. Pino, H. Rothard, E. F. da Silveira, and J. C. Thomas. Swift heavy ion irradiation of water ice from MeV to GeV energies. Approaching true cosmic ray compaction. *Astron. Astrophys.*, 557:A97, September 2013.

[29] R. A. Baragiola. Water ice on outer solar system surfaces: Basic properties and radiation effects. *Planet. Space Sci.*, 51:953–961, December 2003.

[30] E. Dartois, M. Chabot, T. Id Barkach, H. Rothard, B. Augé, A. N. Agnihotri, A. Domaracka, and P. Boduch. Cosmic ray sputtering yield

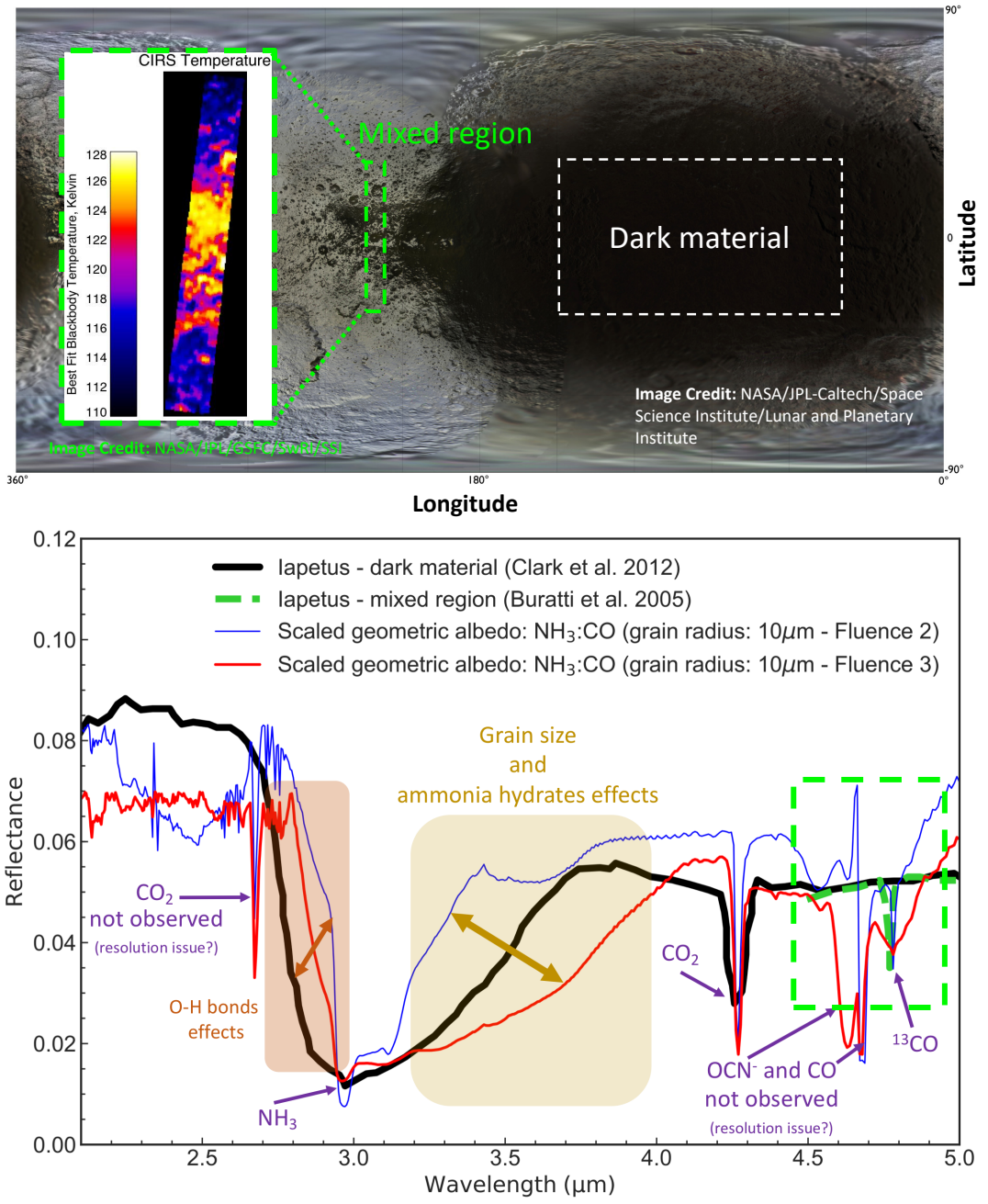

Figure 10: *Top*: Iapetus moon reflectance compared to the scaled geometric albedo of the laboratory data (sample N3# in Table 1). The solid black line indicate the dark material reflectance [61], and the dashed green line, between 4.5–5.0 μm is the reflectance of the mixed region [60]. Both blue and red solid lines are the scaled geometric albedo of NH_3:CO ice mixture, for an icy grain of radius equal to 10μm, and at fluences 2 and 3, respectively. The hatched regions highlight the differences between the experimental and observed data. The dashed green box makes reference to the mixed region shown in the bottom panel. *Bottom*: Global 3-colour map of Iapetus obtained by the Cassini's spacecraft Imaging Science Subsystem (ISS). Both dark material and mixed regions are indicated by the white and green dashed boxes. The subpanel overlayed the bottom panel show the temperature variation for the mixed region, as measured between 9 and 16 μm by the Composite Infrared Spectrometer (CIRS). These images were taken from *https://photojournal.jpl.nasa.gov/target/iapetus*.

of interstellar H_2O ice mantles. Ice mantle thickness dependence. *Astron. Astrophys.*, 618:A173, October 2018.

[31] Koji Ohta and Hatsuo Ishida. Comparison among several numerical integration methods for kramers-kronig transformation. *Appl. Spectrosc.*, 42(6):952–957, Aug 1988.

[32] A. Dawes, N. J. Mason, and H. J. Fraser. Using the C-O stretch to unravel the nature of hydrogen bonding in low-temperature solid methanol-water condensates. *Physical Chemistry Chemical Physics (Incorporating Faraday Transactions)*, 18:1245–1257, 2016.

[33] E. Seperuelo Duarte, P. Boduch, H. Rothard, T. Been, E. Dartois, L. S. Farenzena, and E. F. da Silveira. Heavy ion irradiation of condensed CO_2: sputtering and molecule formation. *Astron. Astrophys.*,

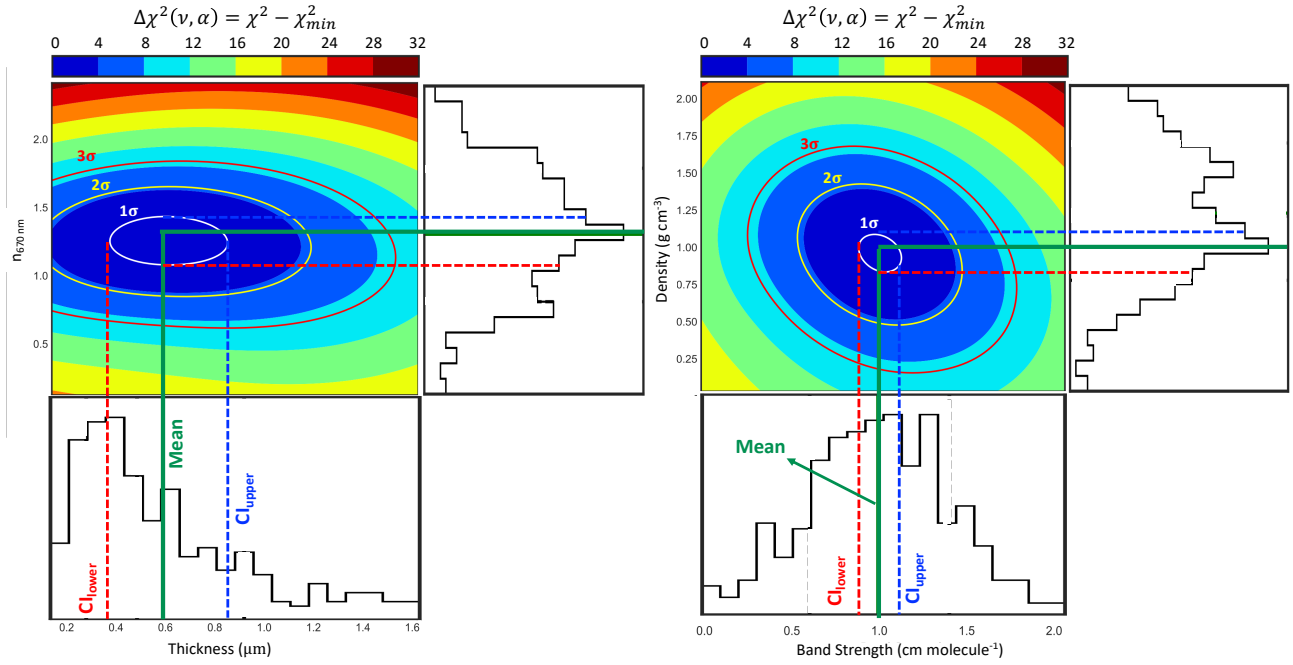

Figure 11: Confidence limit levels and histogram of the input parameters based on a χ^2 statistical analysis. The levels 1-3σ are shown by red, yellow and white solid lines, respectively. The mean is shown by a green solid line, whereas the upper and lower 1σ confidence limits are given by red and blue dashed lines.

502:599–603, August 2009.

[34] P. Boduch, E. Dartois, A. L. F. de Barros, E. F. da Silveira, A. Domaracka, X.-Y. Lv, M. E. Palumbo, S. Pilling, H. Rothard, E. Seperuelo Duarte, and G. Strazzulla. Radiation effects in astrophysical ices. In *Journal of Physics Conference Series*, volume 629 of *Journal of Physics Conference Series*, page 012008, July 2015.

[35] C. Mejía, A. L. F. de Barros, E. Seperuelo Duarte, E. F. da Silveira, E. Dartois, A. Domaracka, H. Rothard, and P. Boduch. Compaction of porous ices rich in water by swift heavy ions. *Icarus*, 250:222–229, April 2015.

[36] H. Rothard, A. Domaracka, P. Boduch, M. E. Palumbo, G. Strazzulla, E. F. da Silveira, and E. Dartois. Modification of ices by cosmic rays and solar wind. *Journal of Physics B Atomic Molecular Physics*, 50(6):062001, March 2017.

[37] M. P. Collings, M. A. Anderson, R. Chen, J. W. Dever, S. Viti, D. A. Williams, and M. R. S. McCoustra. A laboratory survey of the thermal desorption of astrophysically relevant molecules. *Mon. Not. R. Astronom. Soc.*, 354:1133–1140, November 2004.

[38] A. G. G. M. Tielens and W. Hagen. Model calculations of the molecular composition of interstellar grain mantles. *Astron. Astrophys.*, 114:245–260, October 1982.

[39] C. J. Waddington. The ultra heavy elements in the cosmic radiation. *Space Science Reviews*, 130(1):457–464, Jun 2007.

[40] A. E. Glassgold, J. Najita, and J. Igea. X-Ray Ionization of Protoplanetary Disks. *Astrophys. J.*, 480:344–350, May 1997.

[41] B. Müller, B. M. Giuliano, L. Bizzocchi, A. I. Vasyunin, and P. Caselli. O_2 signature in thin and thick O_2-H_2O ices. *Astron. Astrophys.*, 620:A46, November 2018.

[42] C. Knez, M. H. Moore, R. F. Ferrante, and R. L. Hudson. Laboratory IR Studies and Astrophysical Implications of C_2H_2-Containing Binary Ices. *Astrophys. J.*, 748:95, April 2012.

[43] K. M. Pontoppidan, C. P. Dullemond, E. F. van Dishoeck, G. A. Blake, A. C. A. Boogert, N. J. Evans, II, J. E. Kessler-Silacci, and F. Lahuis. Ices in the Edge-on Disk CRBR 2422.8-3423: Spitzer Spectroscopy and Monte Carlo Radiative Transfer Modeling. *Astrophys. J.*, 622:463–481, March 2005.

[44] G. Robinson, R. G. Smith, and M. M. Maldoni. The water-ice librational band: radiative transfer model for AFGL 961. *Monthly Notices of the Royal Astronomical Society*, 424(2):1530–1542, 08 2012.

[45] W. R. M. Rocha and S. Pilling. Computational Modeling of the Class I Low-Mass Protostar Elias 29 Applying Optical Constants of Ices Processed By High Energy Cosmic Ray Analogs. *Astrophys. J.*, 803:18, April 2015.

[46] M. Min, J. Bouwman, C. Dominik, L. B. F. M. Waters, K. M. Pontoppidan, S. Hony, G. D. Mulders, T. Henning, E. F. van Dishoeck, P. Woitke, N. J. Evans, II, and Digit Team. The abundance and thermal history of water ice in the disk surrounding HD 142527 from the DIGIT Herschel Key Program. *Astron. Astrophys.*, 593:A11, August 2016.

[47] I. Kamp, A. Scheepstra, M. Min, L. Klarmann, and P. Riviere-Marichalar. Diagnostic value of far-IR water ice features in T Tauri disks. *Astron. Astrophys.*, 617:A1, September 2018.

[48] W. B. McKinnon, F. Nimmo, T. Wong, P. M. Schenk, O. L. White, J. H. Roberts, J. M. Moore, J. R. Spencer, A. D. Howard, O. M. Umurhan, S. A. Stern, H. A. Weaver, C. B. Olkin, L. A. Young, K. E. Smith, R. Beyer, M. Buie, B. Buratti, A. Cheng, D. Cruikshank, C. Dalle Ore, R. Gladstone, W. Grundy, T. Lauer, I. Linscott, J. Parker, S. Porter, H. Reitsema, D. Reuter, S. Robbins, M. Showalter, K. Singer, D. Strobel, M. Summers, L. Tyler, M. Banks, O. Barnouin, V. Bray, B. Carcich, A. Chaikin, C. Chavez, C. Conrad, D. Hamilton, C. Howett, J. Hofgartner, J. Kammer, C. Lisse, A. Marcotte, A. Parker, K. Retherford, M. Saina, K. Runyon, E. Schindhelm, J. Stansberry, A. Steffl, T. Stryk, H. Throop, C. Tsang, A. Verbiscer, H. Winters, A. Zangari, and G. a. I. T. T. New Horizons Geology. Convection in a volatile nitrogen-ice-rich layer drives Pluto's geological vigour. *Nature*, 534:82–85, June 2016.

[49] M. S. Hanner, R. H. Giese, K. Weiss, and R. Zerull. On the definition of albedo and application to irregular particles. *Astron. Astrophys.*,

104:42–46, December 1981.

[50] C. F. Bohren and D. R. Huffman. *Absorption and scattering of light by small particles*. 1983.

[51] G. Mie. Beiträge zur Optik trüber Medien, speziell kolloidaler Metallösungen. *Annalen der Physik*, 330:377–445, 1908.

[52] H. James Cleaves, Catherine Neish, Michael P. Callahan, Eric Parker, Facundo M. FernÃąndez, and Jason P. Dworkin. Amino acids generated from hydrated titan tholins: Comparison with millerâĂŞurey electric discharge products. *Icarus*, 237:182 – 189, 2014.

[53] C. Sagan and B. N. Khare. Tholins: organic chemistry of interstellar grains and gas. *Nature*, 277(5692):102–107, Jan 1979.

[54] D. P. Cruikshank, W. M. Grundy, D. T. Britt, E. Quirico, B. Schmitt, S. Scipioni, C. M. Dalle Ore, J. C. Cook, L. Gabasova, S. Protopapa, S. A. Stern, H. A. Weaver, A. J. Verbiscer, J. R. Spencer, and New Horizons Composition Team. The Colors of 486958 2014 MU69 ("Ultima Thule"): The Role of Synthetic Organic Solids (Tholins). In *Lunar and Planetary Science Conference*, Lunar and Planetary Science Conference, page 2051, Mar 2019.

[55] A. Leger, S. Gauthier, D. Defourneau, and D. Rouan. Properties of amorphous H2O ice and origin of the 3.1-micron absorption. , 117(1):164–169, Jan 1983.

[56] H. MoosmÃijller and C.M. Sorensen. Small and large particle limits of single scattering albedo for homogeneous, spherical particles. *Journal of Quantitative Spectroscopy and Radiative Transfer*, 204:250 – 255, 2018.

[57] R. H. Brown, K. H. Baines, G. Bellucci, B. J. Buratti, F. Capaccioni, P. Cerroni, R. N. Clark, A. Coradini, D. P. Cruikshank, P. Drossart, V. Formisano, R. Jaumann, Y. Langevin, D. L. Matson, T. B. McCord, V. Mennella, R. M. Nelson, P. D. Nicholson, B. Sicardy, C. Sotin, N. Baugh, C. A. Griffith, G. B. Hansen, C. A. Hibbitts, T. W. Momary, and M. R. Showalter. Observations in the Saturn system during approach and orbital insertion, with Cassini's visual and infrared mapping spectrometer (VIMS). , 446(2):707–716, Feb 2006.

[58] W. M. Grundy, M. W. Buie, J. A. Stansberry, J. R. Spencer, and B. Schmitt. Near-Infrared Spectra of Icy Outer Solar System Surfaces: Remote Determination of H $_2$O Ice Temperatures. , 142(2):536–549, Dec 1999.

[59] Tobias C. Owen, Dale P. Cruikshank, C. M. Dalle Ore, T. R. Geballe, T. L. Roush, C. de Bergh, Roland Meier, Yvonne J. Pendleton, and Bishun N. Khare. Decoding the Domino: The Dark Side of Iapetus. , 149(1):160–172, Jan 2001.

[60] B. J. Buratti, D. P. Cruikshank, R. H. Brown, R. N. Clark, J. M. Bauer, R. Jaumann, T. B. McCord, D. P. Simonelli, C. A. Hibbitts, G. B. Hansen, T. C. Owen, K. H. Baines, G. Bellucci, J. P. Bibring, F. Capaccioni, P. Cerroni, A. Coradini, P. Drossart, V. Formisano, Y. Langevin, D. L. Matson, V. Mennella, R. M. Nelson, P. D. Nicholson, B. Sicardy, C. Sotin, T. L. Roush, K. Soderlund, and A. Muradyan. Cassini Visual and Infrared Mapping Spectrometer Observations of Iapetus: Detection of CO_2. , 622(2):L149–L152, Apr 2005.

[61] Roger N. Clark, Dale P. Cruikshank, Ralf Jaumann, Robert H. Brown, Katrin Stephan, Cristina Morea Dalle Ore, K. Eric Livo, Neil Pearson, John M. Curchin, Todd M. Hoefen, Bonnie J. Buratti, Gianrico Filacchione, Kevin H. Baines, and Philip D. Nicholson. The surface composition of Iapetus: Mapping results from Cassini VIMS. , 218(2):831–860, Apr 2012.